

Geophysical Research Letters

RESEARCH LETTER

10.1029/2021GL092413

Key Points:

- Mid-Infrared Laser Heterodyne Instrument observed intense retrograde winds ($208 \pm 17 \text{ m s}^{-1}$, $159 \pm 20 \text{ m s}^{-1}$, $211 \pm 20 \text{ m s}^{-1}$ on June 21, June 27, August 31, 2018) around 80 km altitude during the 2018 planet-encircling dust event
- We inferred the cause of the intense retrograde winds using a high-resolution numerical model
- The intense retrograde winds can be caused by the enhanced meridional circulation and small-scale gravity waves during the dust event

Supporting Information:

Supporting Information may be found in the online version of this article.

Correspondence to:

H. Nakagawa,
hiromu.nakagawa.c1@tohoku.ac.jp

Citation:

Miyamoto, A., Nakagawa, H., Kuroda, T., Takami, K., Murata, I., Medvedev, A. S., et al. (2021). Intense zonal wind in the Martian mesosphere during the 2018 planet-encircling dust event observed by ground-based infrared heterodyne spectroscopy. *Geophysical Research Letters*, 48, e2021GL092413. <https://doi.org/10.1029/2021GL092413>

Received 13 JAN 2021

Accepted 30 APR 2021

Intense Zonal Wind in the Martian Mesosphere During the 2018 Planet-Encircling Dust Event Observed by Ground-Based Infrared Heterodyne Spectroscopy

Akiho Miyamoto¹ , Hiromu Nakagawa¹ , Takeshi Kuroda¹ , Kosuke Takami¹, Isao Murata¹, Alexander S. Medvedev² , Nao Yoshida¹ , Shohei Aoki^{3,4} , Hideo Sagawa⁵, Yasumasa Kasaba⁶ , and Naoki Terada¹ 

¹Department of Geophysics, Graduate School of Science, Tohoku University, Sendai, Japan, ²Max Planck Institute for Solar System Research, Göttingen, Germany, ³LPAP, STAR Institute, Université de Liège, Liège, Belgium, ⁴Royal Belgian Institute for Space Aeronomy, BIRA-IASB, Brussels, Belgium, ⁵Faculty of Science, Kyoto Sangyo University, Kyoto, Japan, ⁶Planetary Plasma and Atmospheric Research Center, Graduate School of Sciences, Tohoku University, Sendai, Japan

Abstract We report on the direct measurements of zonal winds around 80 km altitude during the 2018 planet-encircling dust event (PEDE) by infrared (IR) heterodyne spectroscopy. The observed Doppler shifts assume intense retrograde (easterly) winds ($208 \pm 17 \text{ m s}^{-1}$, $159 \pm 20 \text{ m s}^{-1}$, $211 \pm 20 \text{ m s}^{-1}$ on June 21, June 27, August 31, 2018, respectively) in the equatorial region during the 2018 PEDE. This is significantly stronger than those during non-storm conditions reported by the previous study (Sonnabend et al., 2012, <https://doi.org/10.1016/j.icarus.2011.11.009>). The substantial retrograde wind during the PEDE is qualitatively consistent with the predictions by the Mars general circulation models (MGCs), however, the observed wind on 31, August, are of a larger magnitude. We evaluated the mechanism of acceleration using the output from a high-resolution MGC. We find out that the stronger winds are related to strengthening the meridional circulation across the equator and forcing by gravity waves.

Plain Language Summary Planet-encircling dust events (PEDE) are spectacular phenomena that occasionally occur in the atmosphere of Mars. The atmospheric circulation on Mars is strongly influenced by dust events, which affect not only the lower atmosphere, but also the mesosphere. The ground-based mid-IR heterodyne spectroscopy was able to observe zonal winds around 80 km during the 2018 PEDE. We found intense retrograde (easterly) winds at the equator, which were much larger than those during non-storm conditions reported by the previous study. This study suggests that the intense retrograde winds during the PEDE were likely caused by the enhanced meridional circulation and small-scale gravity waves.

1. Introduction

Planet-encircling dust events (PEDE) are spectacular phenomena that occasionally occur in the atmosphere of Mars. They substantially change the global circulation and transport processes in the entire atmosphere (Medvedev et al., 2011; Smith et al., 2002). In particular, recent observations with the ExoMars Trace Gas Orbiter (TGO) found increased abundances of water vapor at altitudes up to 100 km during the 2018 PEDE (Aoki et al., 2019; Fedorova et al., 2020; Vandaele et al., 2019). Simulations with three-dimensional Mars general circulation models (MGCs) corroborated these observations and linked the increase of high-altitude water vapor to the enhanced transport by the meridional circulation during the major dust events in 2007 (Shaposhnikov et al., 2019) and 2018 (Neary et al., 2020). The presence of water at such high altitudes can explain the previously observed increase of the hydrogen corona in the upper thermosphere (Bhat-tacharyya et al., 2015; Clarke et al., 2017) and an intensified loss of water from Mars to space due to its photo-dissociation to hydrogen (Chaffin et al., 2017; Heavens et al., 2018).

Although the atmospheric circulation on Mars is strongly influenced by dust events, observational constraints on mesospheric winds are limited. Heterodyne spectroscopy at millimeter or infrared (IR) wavelengths with high spectral resolution $\left(\frac{\nu}{\Delta\nu} \sim 10^7\right)$ can be used for probing the Martian mesosphere,

Table 1
Observation Parameters

Date (2018)	L_s (°)	Relative velocity (km s ⁻¹)	Apparent diameter of Mars (arcsec)	Observed longitude (°E)	Observed local time	Integration time on each of the two targeted positions (min)
21 June	197	-8.8	19.0	63–62 (limb)	7:45 (limb)	10
				159–143 (center)	13:45 (center)	
27 June	201	-7.6	20.2	87–57 (limb)	7:30 (limb)	60
				170–166 (center)	13:30 (center)	
31 August	241	6.6	21.0	168–163 (limb)	16:15 (limb)	20
				123–82 (center)	10:00 (center)	

allowing for wind measurements from Doppler-shifted molecular lines. There were only a few attempts to apply this instrumentation on Mars (e.g., Cavalié et al., 2008; Lellouch et al., 1991; Moreno et al., 2009; Sonnabend et al., 2012). Moreno et al. (2009) observed the zonal wind during the 2001 PEDE by measuring the CO(1–0) line using the IRAM Plateau de Bure Interferometer. They detected a prograde (westerly) wind of ~ 30 m s⁻¹ around 50 km during the dust event. At higher altitude, Sonnabend et al. (2012) employed the IR heterodyne spectroscopy and reported the zonal wind velocities around 80 km measured around the northern spring equinox during Martian Years (MY) 27 and 29 with values less than 100 m s⁻¹ retrograde (easterly) around the equator for wind going from east to west on the planet.

Note that the region around 80 km remains the least explored, although its highly variable nature deserves extensive observations, especially during dust storms. In June 2018, during MY34, a PEDE occurred on Mars, which provided a rare opportunity to measure the mesospheric dynamics during PEDEs. We performed direct measurements of zonal winds around 80 km by ground-based IR heterodyne spectroscopy. The dust event continued from $L_s = 195^\circ$ – 260° (Aoki et al., 2019). We were able to obtain the data from June–August 2018 ($L_s = 197^\circ$ – 241°).

2. Observations

The observations were carried out using the Mid-Infrared Laser Heterodyne Instrument (MILAH) (Nakagawa et al., 2016) mounted to the Tohoku University 60 cm telescope (T60) at the summit of Mt. Haleakala, Hawaii. In the MILAH instrument, the IR light from the telescope is mixed with the CO₂ gas laser as the local oscillator at the ZnSe beam splitter, and focused onto the Mercury-Cadmium-Telluride (MCT) photodiode mixer. In this observation, we observed 10 μ m non-Local Thermal Equilibrium (LTE) CO₂ emission line. Each observation includes a single CO₂ line within its bandwidth (2.5 GHz). The measured wavelengths of CO₂ non-LTE emission were 10.591 μ m, 10.532 μ m, and 10.513 μ m on June 21, June 27, August 31, 2018, respectively.

Table 1 summarizes the observational parameters applied in this study: the dates, solar longitudes (L_s), relative velocity between Earth and Mars, apparent diameter of Mars, longitude, local time on Mars, and integration time. During the observations in June–August 2018, the Martian season varied from late spring to early summer in the southern hemisphere ($L_s = 197^\circ$ – 241°). The Earth-Mars Doppler shift varied from -8.8 to 6.6 km s⁻¹.

Figure 1 shows the observing geometry with the positions of the field-of-view (FOV) scaled to the planetary diameter. Hereafter, we define the FOV to be approximately FWHM of the beam. The apparent diameter of Mars over the observing period varied from 19.0 to 21.0 arcsec, compared to the diffraction-limited FOV of the telescope of 4.4 arcsec. We measured CO₂ non-LTE emission spectra, both at the Martian disk center and equatorial limb, on the dayside for 3 days, 21 June, 27 June, and 31 August. The acquisition time for an individual spectrum was ~ 5 min. The integration time given in Table 1 corresponds to the summation of 2, 12, and 4 individual measurements of 5 min acquisition time in each instance on 21, 27 June, and 31 August, respectively, on each of the two targeted positions.

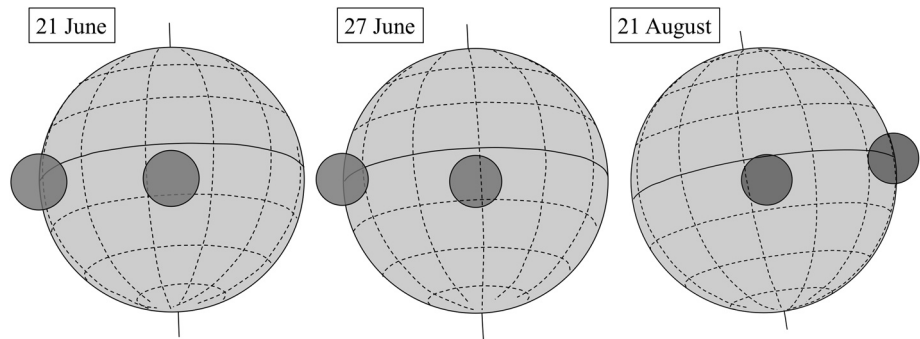


Figure 1. The observing geometry of Mars on June 21, June 27, August 31, 2018. The dark-shading circles shows the pointing positions on Mars, with the size of diffraction-limited field-of-view.

The spectra were taken both on and off Mars using two beam paths. The on-source (Mars) signal acquisition was alternated between two-beam paths to minimize systematic characteristics, the technique well known in radio astronomy as a “double beam switch” (Sonnabend et al., 2006).

In order to increase the signal-to-noise ratio, an individual spectrum at the disk center and equatorial limb was separately averaged during each date by shifting its frequency according to the relative velocity between Earth and Mars. The relative timing for when the spectra were acquired for each targeted positions can be found in Figures S1–S6 in the supporting information (SI). The averaged CO₂ non-LTE emission line is fitted by the Gaussian function in the frequency range of about ± 100 MHz from the spectral peak of the CO₂ line (see Figure 2). The surrounding spectral feature is fitted by a second-order curve as the baseline. The Doppler shift due to the solid rotation (240 m s^{-1} at the equator) of the planet was then, subtracted. The line-of-sight velocity of the solid rotation varies within the finite size of FOV, which is taken into consideration in this correction. The Doppler shift at the Mars disk center is used as the reference of the line-of-sight velocity of zonal wind (i.e., no vertical winds are assumed). The derived line-of-sight wind velocity at the

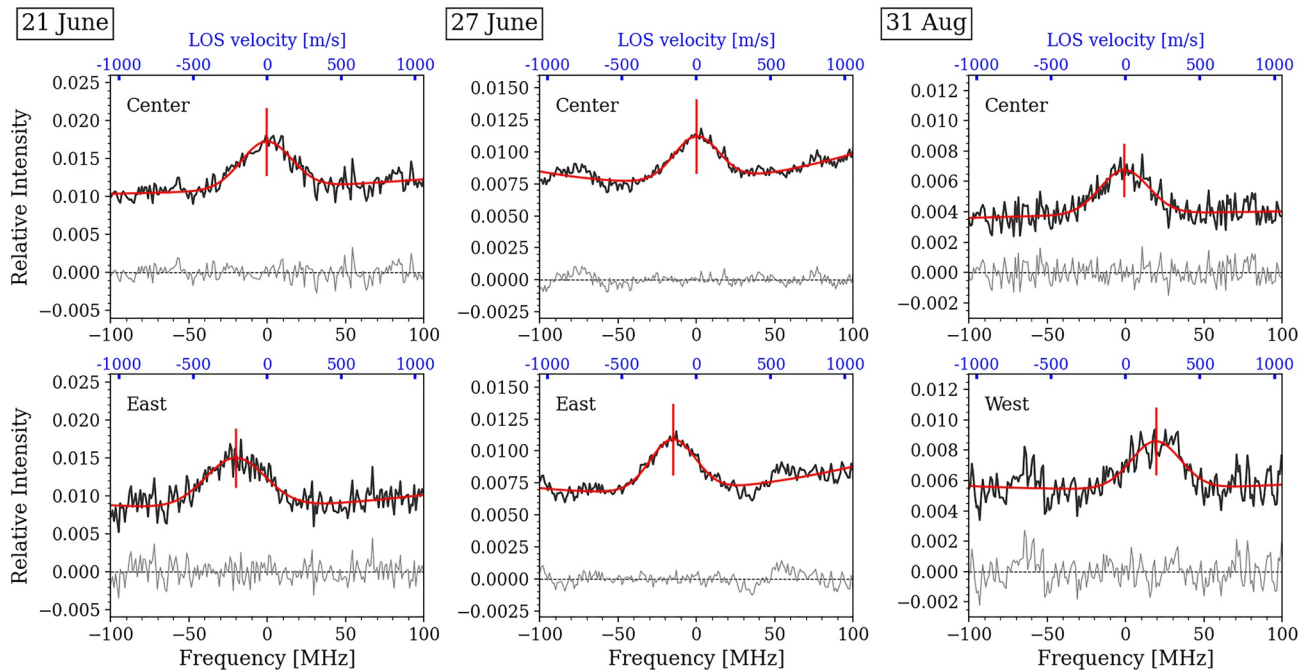


Figure 2. Observed spectra (black) of CO₂ non-Local Thermal Equilibrium emission lines at $10 \mu\text{m}$ and the best-fit curves (red). The residuals between the observed spectrum and the best-fit are also shown in gray spectra. Upper and lower panels show the spectra from the disk center and equatorial limb, respectively. The abscissa represents Doppler shifts by frequency offset (bottom ticks) and line-of-sight velocity (upper ticks). The determined line position is indicated with a vertical line.

Table 2
The Observed Zonal Winds (With Positive Values Indicating Retrograde Winds) and the 1-Sigma Fitting Errors

	June 21, 2018 (MY34, $L_s = 197^\circ$)	27 June ($L_s = 201^\circ$)	31 August ($L_s = 241^\circ$)
Doppler shift (MHz)	-19.7 ± 1.2	-15.1 ± 0.7	20.1 ± 1.5
Wind velocity (m s^{-1})	208 ± 12	159 ± 7	211 ± 16

of the spectral peak between the disk center and the limb measurements. After subtracting the Doppler shift by the relative velocity between Earth and Mars, the stability of the emission frequency at the disk center has been evaluated for each date. We confirmed the stability of the emission frequency at the disk center during the observing time in three days. The estimated uncertainty of the emission frequency position in the disk center measurements (i.e., the reference for zero-velocity of zonal wind) is less than 5 m s^{-1} for 21 June, 31 August, and is about 15 m s^{-1} on 27 June. Meanwhile, we have to note that the absolute value of the emission frequency at the disk center systematically had an offset from the prediction. The magnitudes of the offset are 26.8 MHz on 21 June, 42.8 MHz on 27 June, and 29.7 MHz on 31 August, on average. We do not have a clear explanation for the discrepancy, which might be due to a systematic error in the frequency calibration. This study, thus, places more emphasis on the differential velocity measurements (between the disk center and limb), since that is unaffected by a systematic issue of this sort.

3. Results

Figure 2 presents the observed spectra at the Martian disk center (upper panels) and equatorial limb (lower panels). The best-fit Gaussian line shape is shown in the red curve with clarifying the line position by a vertical line. The labels in the upper abscissa show the line-of-sight velocity, converted from the Doppler shift labeled in the lower abscissa. The fitted frequency offset were then, converted to zonal wind velocities. The observed Doppler shift assume intense retrograde (easterly) winds of $208 \pm 12 \text{ m s}^{-1}$, $159 \pm 7 \text{ m s}^{-1}$, $211 \pm 16 \text{ m s}^{-1}$ on June 21, June 27, August 31, 2018, respectively (summarized in Table 2). The uncertainty is estimated from the standard deviation of the fitting. Our results showed that the mesospheric winds were retrograde during the PEDE in all of the cases, which is consistent with the direction from the previous study during non-storm conditions (Sonnabend et al., 2012). In contrast, the amplitudes of the derived wind velocities are strikingly different (see the magnitude of the difference in Figure 3). Our results show large Doppler shifts corresponding to significantly stronger winds with respect to non-storm conditions (Sonnabend et al., 2012).

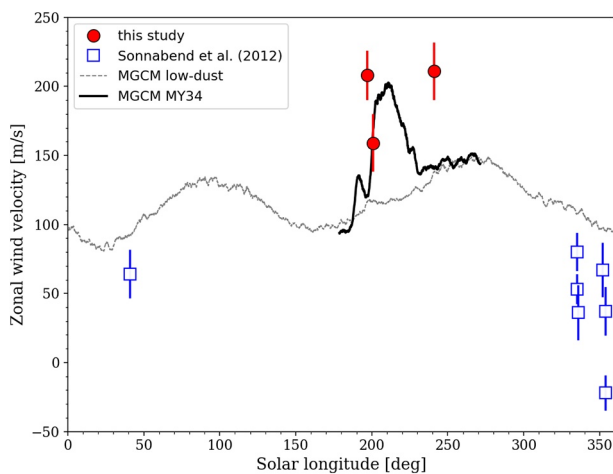


Figure 3. Temporal variation of the observed zonal wind velocities (red circles). The errors were estimated using the Root Sum Square due to the $1\text{-}\sigma$ fitting errors, uncertainties in the frequency calibration and the reference frequency determination, and variation of relative velocity during the acquisition time. The winds reported by a previous study (Sonnabend et al., 2012) are shown as square symbols for their corresponding season. The maximum equatorial retrograde wind velocities obtained by a Mars general circulation model for the corresponding season during the Planet-encircling dust events (PEDE) (solid line) and those without the PEDE (dashed line) are imposed.

equatorial limb is interpreted as the amplitude zonal winds. The validity of this interpretation is discussed in the next section.

The frequency reference of the CO_2 gas laser was simultaneously obtained by the monochrometer. The optical path of the CO_2 gas laser was divided into two beams by an additional beam splitter. The diffraction grating determines the frequency reference. An individual spectrum has been carefully investigated, as shown in Figures S1–S6 (see SI for more details). The relevant variation of the individual emission frequency at the disk center well agreed with the predicted relative velocity between Earth and Mars. Therefore, we have confidence in the relative variation

of the spectral peak between the disk center and the limb measurements. After subtracting the Doppler shift by the relative velocity between Earth and Mars, the stability of the emission frequency at the disk center has been evaluated for each date. We confirmed the stability of the emission frequency at the disk center during the observing time in three days. The estimated uncertainty of the emission frequency position in the disk center measurements (i.e., the reference for zero-velocity of zonal wind) is less than 5 m s^{-1} for 21 June, 31 August, and is about 15 m s^{-1} on 27 June. Meanwhile, we have to note that the absolute value of the emission frequency at the disk center systematically had an offset from the prediction. The magnitudes of the offset are 26.8 MHz on 21 June, 42.8 MHz on 27 June, and 29.7 MHz on 31 August, on average. We do not have a clear explanation for the discrepancy, which might be due to a systematic error in the frequency calibration. This study, thus, places more emphasis on the differential velocity measurements (between the disk center and limb), since that is unaffected by a systematic issue of this sort.

Figure 2 presents the observed spectra at the Martian disk center (upper panels) and equatorial limb (lower panels). The best-fit Gaussian line shape is shown in the red curve with clarifying the line position by a vertical line. The labels in the upper abscissa show the line-of-sight velocity, converted from the Doppler shift labeled in the lower abscissa. The fitted frequency offset were then, converted to zonal wind velocities. The observed Doppler shift assume intense retrograde (easterly) winds of $208 \pm 12 \text{ m s}^{-1}$, $159 \pm 7 \text{ m s}^{-1}$, $211 \pm 16 \text{ m s}^{-1}$ on June 21, June 27, August 31, 2018, respectively (summarized in Table 2). The uncertainty is estimated from the standard deviation of the fitting. Our results showed that the mesospheric winds were retrograde during the PEDE in all of the cases, which is consistent with the direction from the previous study during non-storm conditions (Sonnabend et al., 2012). In contrast, the amplitudes of the derived wind velocities are strikingly different (see the magnitude of the difference in Figure 3). Our results show large Doppler shifts corresponding to significantly stronger winds with respect to non-storm conditions (Sonnabend et al., 2012).

Figure 3 shows temporal variations of the observed zonal wind velocities. The errors were estimated using the Root Sum Square due to the $1\text{-}\sigma$ fitting errors (see Table 2), frequency calibration provided through a reference gas cell ($\sim 10 \text{ m s}^{-1}$), uncertainty in the determination of the reference frequency for zero-velocity (see SI for detail), and variation of relative velocity during the acquisition time. The errors due to the variation of relative velocity during the acquisition time are ± 4.3 to $\pm 5.4 \text{ m s}^{-1}$. Total magnitude of the random errors are 17 m s^{-1} , 20 m s^{-1} , 20 m s^{-1} on June 21, June 27, August 31, 2018, respectively.

As a possible systematic error, we raise a point that the limb measurements include a certain extent of “nadir” contribution within its FOV. The line-of-sight velocity of a zonal wind decreases when the observation

geometry approaches a nadir pointing. For our measurements, if this geometrical effect is simply applied, direct interpretation of the line-of-sight velocity from the limb spectra as a zonal wind velocity underestimates the actual zonal wind by $\sim 20\%$.

One must also consider the fact that the radiance of CO_2 non-LTE emission largely depends on the solar zenith angle and the line-of-sight's tangent height of observation (López-Valverde et al., 2016). Basically, the emission at the dayside limb is much brighter compared to the nadir one. Such a radiance variation within a FOV plays a weight of the contribution of different observation geometries. We calculated the effective underestimation factor as $\sim 15\%$ by using a generic formula of the CO_2 non-LTE radiance modeling (López-Valverde et al., 2016),

Even considering the uncertainty, the comparison with the previous study at non-storm conditions (e.g., Sonnabend et al., 2012) reveals the presence of a substantial retrograde zonal wind during the PEDE. For comparison, the winds in the equatorial region ($<20^\circ$ in latitudes) reported by previous study (Sonnabend et al., 2012) are also shown in Figure 3 as cross dots for their corresponding season. To discriminate the effect of PEDE from the nominal seasonal variation, we checked the zonal winds from MGCMs. The maximum equatorial retrograde wind velocities obtained by an MGCM with a horizontal resolution of $\sim 1.1^\circ$ in both longitude and latitude (Kuroda et al., 2019, 2020) for the corresponding season are imposed on Figure 3. The wind velocities shown here are the zonal (diurnal) and meridional maximum easterly velocities averaged in 75–85 km geopotential height and 10° in longitude and latitude within the central latitudes of less than 20° , followed by the time smoothing for five sols. The MGCM predicts that the retrograde wind velocity possibly increases up to $\sim 200 \text{ m s}^{-1}$ during the PEDE, $\sim 85 \text{ m s}^{-1}$ faster than the case without the PEDE. Also, the MGCM predicts the increase of the velocity according to the progress of L_s from the equinox to the southern summer solstice, which possibly explains the qualitative increase of the observed velocity.

4. Discussion

The observed enhancement of the retrograde (easterly) equatorial wind in the mesosphere during dust storms has been captured by the MGCMs (Kuroda et al., 2020; Medvedev et al., 2013; Ruan et al., 2019). Medvedev et al. (2013), with a horizontal resolution of $\sim 5.6^\circ$ in both longitude and latitude and a gravity wave drag parameterization empirical for terrestrial thermosphere (Yigit et al., 2008), presented simulations based on the zonally averaged dust distributions observed by the Thermal Emission Spectrometer instrument (TES) onboard the Mars Global Surveyor (MGS) during the 2001 PEDE (MY25), which started at almost the same season as the one in 2018. In the equatorial region at our observed altitude ($\sim 0.1 \text{ Pa}$ pressure level), they showed an easterly acceleration of the zonal-mean wind averaged over $L_s = 190^\circ\text{--}200^\circ$ as $>70 \text{ m s}^{-1}$ in comparison with the results for the low-dust conditions (Medvedev et al., 2013, Figure 5). Ruan et al. (2019, Figure 1d) presented the annual data-assimilated MGCM simulations of the equatorial wind for the MY25 dust conditions. They also found a sudden increase of the easterly wind in the mesosphere during the storm (exceeding 80 m s^{-1}) as compared to non-PEDE years (MY24 and MY26). Indeed, Kuroda et al. (2008, Figure 2) showed that even a regional dust storm in southern spring as observed in MY24 affect the acceleration of the easterly wind for $>100 \text{ m s}^{-1}$.

Recently, Kuroda et al. (2020) performed MGCM simulations with a higher horizontal resolutions and the gravity wave drag parameterizations eliminated using the dust scenario for the 2018 PEDE, as plotted in Figure 3. They demonstrated an enhancement (and rapid vertical descent, similar to the feature seen in Ruan et al., 2019 for MY25) of the equatorial easterlies at $\sim 0.1 \text{ Pa}$ from $L_s \sim 195^\circ$ which corresponds to a few days after the onset of the storm (Kuroda et al., 2020, Figure 6b). A second enhancement of the easterlies occurred later (before $L_s = 240^\circ$), which was associated with the seasonal change, as can be judged from the simulation for a low-dust condition (Kuroda et al., 2020, Figure 6a). Note that the timing of the enhancements is close to that of the presented observations.

There are two elements which may contribute to the easterly wind acceleration due to the PEDE. One is the enhancement of meridional circulation. As indicated in Medvedev et al. (2013), the PEDE enhances the meridional circulation due to the radiative heating by airborne dust. The mean zonal wind acceleration rate $\partial \bar{u} / \partial t$ on the equator can be estimated by the transformed Eulerian mean (TEM) formulation (Andrews et al., 1987) as follows (the Coriolis parameter is ignored and the cosine of the latitude is assumed as unity),

$$\frac{\partial \bar{u}}{\partial t} = -\frac{1}{a} \bar{v}^* \bar{u}_\phi - \bar{w}^* \bar{u}_z + \frac{\nabla \cdot \mathbf{F}}{\rho_0 a}, \quad (1)$$

where $(0, \bar{v}^*, \bar{w}^*)$ are the residual mean meridional and vertical velocities, overbars denote zonal averaging, $a = 3.396 \times 10^6$ m is the radius of Mars, ϕ is the latitude, $\mathbf{F} = \left(0, \bar{u}_z \bar{v}' \bar{\theta}' \bar{\theta}_z^{-1} - \bar{v}' \bar{u}', a^{-1} \bar{u}_\phi \bar{v}' \bar{\theta}' \bar{\theta}_z^{-1} - \bar{w}' \bar{u}'\right)$ is the Eliassen-Palm (EP) flux due to non-zonal eddies, θ is the potential temperature, primes denote deviations from the zonal-mean values, and ρ_0 is the atmospheric reference density. In northern autumn with the mid-litudinal westerly jet in the northern hemisphere \bar{u}_ϕ is kept to be positive, so the larger \bar{v}^* on equator the larger the easterly acceleration occurs. From the MGCM results of Kuroda et al. (2019, 2020), the value of the first term of Equation 1 averaged in 75–85 km altitude on equator is approximately $-30 \text{ m s}^{-1} \text{ sol}^{-1}$ (note that the positive value denote the acceleration rate of westerly wind, so this shows the contribution to the easterly wind acceleration), while $-10 \text{ m s}^{-1} \text{ sol}^{-1}$ in the calculations for the same season without a PEDE.

The other is the effect of gravity wave activities. As discussed in Kuroda et al. (2020), the change of background zonal wind fields should make the gravity waves in a greater part of the incident spectrum favorably propagate to the upper atmosphere. The acceleration rate of zonal wind velocity due to the gravity waves is proportional to the vertical dissipation rate of wave horizontal momentum $u'w'$, as represented in the third term of Equation 1. Substituting $u'w'$ to the one by small-scale gravity waves (with horizontal total wavenumber of larger than 60, or wavelengths of shorter than ~ 350 km) simulated in the MGCM (Kuroda et al., 2019, 2020), the acceleration rate by gravity waves is approximately $-30 \text{ m s}^{-1} \text{ sol}^{-1}$ during the 2018 PEDE, while almost zero without a PEDE. Consequently, the large contribution to the acceleration of the equatorial easterlies comes from the mean meridional circulation and gravity waves, which results in the faster estimated equatorial easterly wind velocity for up to $\sim 85 \text{ m s}^{-1}$ during the 2018 PEDE.

However, as seen in Figure 3, even the diurnal maximum values of equatorial easterlies in the MGCM are below the observed ones. Some other mechanisms could be at play, and further observations are required to constrain the mesospheric dynamics.

Finally, we have to note that the measured wind velocities maintain its high values on 31 August as seen in Figure 3; while, the dust storm was significantly weaker by the end of August (Fedorova et al., 2020; Lugnin et al., 2020). According to the model prediction by Kuroda et al. (2020), the impact of dust storms on the zonal winds is essentially the same regardless of the extent of the storm. The discrepancy between our result and dust storm evolution might suggest a bias of the wind determination in our result. One might need to note that the additional water vapor enhancement occurs even at the decay phase ($L_s \sim 240$) (Aoki et al., 2019). Further observations are needed for validation of this study and clarifying its evolution before/after PEDE.

5. Conclusions

We directly derived the line-of-sight wind velocities around 80 km during the 2018 PEDE from the Doppler shift of the transition lines of $10 \mu\text{m}$ non-LTE CO_2 emission. The presented data set provides a first view of the dynamics of the middle atmosphere of Mars during PEDEs. The results were significantly stronger than those during non-storm conditions reported by the previous ground-based measurements (Sonnabend et al., 2012). The substantial retrograde wind during the PEDE is qualitatively consistent with the predictions by MGCMs that employed dust distributions corresponding to the 2001 and 2018 PEDE (Medvedev et al., 2013; Ruan et al., 2019). Our result suggests that the stronger winds during a PEDE are related to strengthening the meridional circulation across the equator and forcing by gravity waves.

Data Availability Statement

The MGCM data supporting the figures and discussions are available at Kuroda (2019a, 2019b, 2020). The observational data supporting the figures and discussions are available at Miyamoto (2021).

Acknowledgments

This work was supported by the Grant-in-Aid for Scientific Research (A) 19H00707, (B) 15H05209, (C) JP19K03943, JP19K03980, and JP20K04046 from JSPS, and Grant-in-Aid for Scientific Research on Innovative Areas for No. 20H04605 from JSPS. This work was carried out by the joint research program of the Institute for Space-Earth Environmental Research, Nagoya University. S. Aoki is “Chargé de Recherches” of the F.R.S.-FNRS.

References

- Andrews, D. G., Holton, J. R., & Leovy, C. B. (1987). Middle atmosphere dynamics (International Geophysics Series, Vol. 40, p. 489). Academic.
- Aoki, S., Vandaele, A. C., Daerden, F., Villanueva, G. L., Liuzzi, G., Thomas, I. R., et al. (2019). Water vapor vertical profiles on Mars in dust storms observed by TGO/NOMAD. *Journal of Geophysical Research: Planets*, *124*, 3482–3497. <https://doi.org/10.1029/2019JE006109>
- Bhattacharyya, D., Clarke, J. T., Bertaux, J.-L., Chaufray, J.-Y., & Mayyasi, M. (2015). A strong seasonal dependence in the Martian hydrogen exosphere. *Geophysical Research Letters*, *42*, 8678–8685. <https://doi.org/10.1002/2015GL065804>
- Cavalié, T., Billebaud, F., Encrenaz, T., Dobrijevic, M., Brillet, J., Forget, F., & Lellouch, E. (2008). Vertical temperature profile and mesospheric winds retrieval on Mars from CO millimeter observations. *Astronomy & Astrophysics*, *489*, 795–809. <https://doi.org/10.1051/0004-6361/200809815>
- Chaffin, M. S., Deighan, J., Schneider, N. M., & Stewart, A. I. F. (2017). Elevated atmospheric escape of atomic hydrogen from Mars induced by high-altitude water. *Nature Geoscience*, *10*, 174–178. <https://doi.org/10.1038/ngeo2887>
- Clarke, J. T., Mayyasi, M., Bhattacharyya, D., Schneider, N. M., McClintock, W. E., Deighan, J. I., et al. (2017). Variability of D and H in the Martian upper atmosphere observed with the MAVEN IUVs Echelle channel. *Journal of Geophysical Research: Space Physics*, *122*, 2336–2344. <https://doi.org/10.1002/2016JA023479>
- Fedorova, A. A., Montmessin, F., Korabiev, O., Luginin, M., Trokhimovskiy, A., Belyaev, D. A., et al. (2020). Stormy water on Mars: The distribution and saturation of atmospheric water during the dusty season. *Science*, *367*, 297–300. <https://doi.org/10.1126/science.aay9522>
- Heavens, N. G., Kleinböhl, A., Chaffin, M. S., Halekas, J. S., Kass, D. M., Hayne, P. O., et al. (2018). Hydrogen escape from Mars enhanced by deep convection in dust storms. *Nature Astronomy*, *2*, 126–132. <https://doi.org/10.1038/s41550-017-0353-4>
- Kuroda, T. (2019a). Dataset of “annual cycle of gravity wave variability derived from a high-resolution martian general circulation model” (2/3) (Data set). Zenodo. <https://doi.org/10.5281/zenodo.2578744>
- Kuroda, T. (2019b). Dataset of “annual cycle of gravity wave variability derived from a high-resolution martian general circulation model” (3/3) (Data set). Zenodo. <https://doi.org/10.5281/zenodo.2578764>
- Kuroda, T. (2020). Dataset of gravity wave activity in the atmosphere of Mars during the 2018 global dust storm: Simulations with a high-resolution model (Data set). Zenodo. <https://doi.org/10.5281/zenodo.4047700>
- Kuroda, T., Medvedev, A. S., Hartogh, P., & Takahashi, M. (2008). Semiannual oscillations in the atmosphere of Mars. *Geophysical Research Letters*, *35*, L23202. <https://doi.org/10.1029/2008GL036061>
- Kuroda, T., Medvedev, A. S., & Yiğit, E. (2020). Gravity wave activity in the atmosphere of Mars during the 2018 global dust storm: Simulations with a high-resolution model. *Journal of Geophysical Research: Planets*, *125*, e2020JE006556. <https://doi.org/10.1029/2020JE006556>
- Kuroda, T., Yiğit, E., & Medvedev, A. S. (2019). Annual cycle of gravity wave activity derived from a high-resolution martian general circulation model. *Journal of Geophysical Research: Planets*, *124*, 1618–1632. <https://doi.org/10.1029/2018JE005847>
- Lellouch, E., Rosenqvist, J., Goldstein, J. J., Paubert, S. W. G., & Rosenqvist, J. (1991). First absolute wind measurements in the middle atmosphere of Mars. *Acta Pathologica Japonica*, *383*, 401–406. <https://doi.org/10.1086/170797>
- Lopez-Valverde, M. A., Montabone, L., Sornig, M., & Sonnabend, G. (2016). On the retrieval of mesospheric winds on Mars and Venus from ground-based observations at 10 μm. *Acta Pathologica Japonica*, *816*, 103. <https://doi.org/10.3847/0004-637X/816/2/103>
- Luginin, M., Fedorova, A., Ignatiev, N., Trokhimovskiy, A., Shakun, A., Grigoriev, A., et al. (2020). Properties of water ice and dust particles in the atmosphere of Mars during the 2018 global dust storm as inferred from the Atmospheric Chemistry Suite. *Journal of Geophysical Research*, e2020JE006419. <https://doi.org/10.1029/2020JE006419>
- Medvedev, A. S., Yiğit, E., & Hartogh, P. (2011). General circulation modeling of the Martian upper atmosphere during global dust storms. *Journal of Geophysical Research*, *118*, 2234–2246. <https://doi.org/10.1002/2013JE004429>
- Medvedev, A. S., Yiğit, E., Kuroda, T., & Hartogh, P. (2013). General circulation modeling of the Martian upper atmosphere during global dust storms. *Journal of Geophysical Research: Planets*, *118*, 2234–2246. <https://doi.org/10.1002/2013JE004429>
- Miyamoto, A., & Nakagawa, H. (2021). Spectral data used in the paper intense zonal wind in the martian mesosphere during the 2018 planet encircling dust event observed by ground-based IR heterodyne spectroscopy (Data set). Zenodo. <https://doi.org/10.5281/zenodo.4700655>
- Moreno, R., Lellouch, E., Forget, F., Encrenaz, T., Guilloteau, S., & Millour, E. (2009). Wind measurements in Mars’ middle atmosphere: IRAM Plateau de Bure interferometric CO observations. *Icarus*, *201*(2), 549–563. <https://doi.org/10.1016/j.icarus.2009.01.027>
- Nakagawa, H., Aoki, S., Sagawa, H., Kasaba, Y., Murata, I., Sonnabend, G., et al. (2016). IR heterodyne spectrometer MILAHI for continuous monitoring observatory of Martian and Venusian atmospheres at Mt. Haleakalā, Hawaii. *Planetary and Space Science*, *126*, 34–48. <https://doi.org/10.1016/j.pss.2016.04.002>
- Neary, L., Daerden, F., Aoki, S., Whiteway, J., Clancy, R. T., Smith, M., et al. (2020). Explanation for the increase in high-altitude water on Mars observed by nomad during the 2018 global dust storm. *Geophysical Research Letters*, *47*, e2019GL084354. <https://doi.org/10.1029/2019GL084354>
- Ruan, T., Lewis, N. T., Lewis, S. R., Montabone, L., & Read, P. L. (2019). Investigating the semiannual oscillation on Mars using data assimilation. *Icarus*, *333*(15), 404–414. <https://doi.org/10.1016/j.icarus.2019.06.012>
- Shaposhnikov, D. S., Medvedev, A. S., Rodin, A. V., & Hartogh, P. (2019). Seasonal water “pump” in the atmosphere of Mars: Vertical transport to the thermosphere. *Geophysical Research Letters*, *46*, 4161–4169. <https://doi.org/10.1029/2019GL082839>
- Smith, M., Conrath, B. J., Pearl, J. C., & Christensen, P. (2002). Thermal emission spectrometer observations of Martian planet-encircling dust storm 2001A. *Icarus*, *157*(1), 259–263. <https://doi.org/10.1006/icar.2001.6797>
- Sonnabend, G., Sornig, M., Kroetz, P. J., & Stupar, D. (2012). Mars mesospheric zonal wind around northern spring equinox from infrared heterodyne observations of CO₂. *Icarus*, *217*(1), 315–321. <https://doi.org/10.1016/j.icarus.2011.11.009>
- Sonnabend, G., Sornig, M., Krötz, P. J., Schieder, R. T., & Fast, K. E. (2006). High spatial resolution mapping of Mars mesospheric zonal winds by infrared heterodyne spectroscopy of CO₂. *Geophysical Research Letters*, *33*, L18201. <https://doi.org/10.1029/2006GL026900>
- Vandaele, A. C., Korabiev, O., Daerden, F., Aoki, S., Thomas, I. R., Altieri, F., et al. (2019). Martian dust storm impact on atmospheric H₂O and D/H observed by ExoMars Trace Gas Orbiter. *Nature*, *568*, 521–525. <https://doi.org/10.1038/s41586-019-1097-3>
- Yiğit, E., Aylward, A. D., & Medvedev, A. S. (2008). Parameterization of the effects of vertically propagating gravity waves for thermosphere general circulation models: Sensitivity study. *Journal of Geophysical Research*, *113*, D19106. <https://doi.org/10.1029/2008JD010135>